Phys. Med. Biol. **44** (1999) 607–624. Printed in the UK PII: S0031-9155(99)94798-X

Comparison of four magnetic resonance methods for mapping small temperature changes

Waldemar Wlodarczyk†‡§, Michael Hentschel†, Peter Wust†, Ralf Noeske‖, Norbert Hosten†, Herbert Rinneberg‖ and Roland Felix†

† Clinic for Radiation Medicine, Charité Medical School—Campus Virchow-Klinikum, 13353 Berlin, Germany
‡ Department of Electrical Engineering, Technical University, 10587 Berlin, Germany
‖ Physikalisch-Technische Bundesanstalt, Berlin-Charlottenburg, 10587 Berlin, Germany

Received 3 June 1998, in final form 24 November 1998

Abstract. Non-invasive detection of small temperature changes (<1 °C) is pivotal to the further advance of regional hyperthermia as a treatment modality for deep-seated tumours. Magnetic resonance (MR) thermography methods are considered to be a promising approach. Four methods exploiting temperature-dependent parameters were evaluated in phantom experiments. The investigated temperature indicators were spin–lattice relaxation time T_1, diffusion coefficient D, shift of water proton resonance frequency (water PRF) and resonance frequency shift of the methoxy group of the praseodymium complex (Pr probe). The respective pulse sequences employed to detect temperature-dependent signal changes were the multiple readout single inversion recovery (T One by Multiple Read Out Pulses; TOMROP), the pulsed gradient spin echo (PGSE), the fast low-angle shot (FLASH) with phase difference reconstruction, and the classical chemical shift imaging (CSI). Applying these sequences, experiments were performed in two separate and consecutive steps. In the first step, calibration curves were recorded for all four methods. In the second step, applying these calibration data, maps of temperature changes were generated and verified. With the equal total acquisition time of approximately 4 min for all four methods, the uncertainties of temperature changes derived from the calibration curves were less than 1 °C (Pr probe 0.11 °C, water PRF 0.22 °C, D 0.48 °C and T_1 0.93 °C). The corresponding maps of temperature changes exhibited slightly higher errors but still in the range or less than 1 °C (0.97 °C, 0.41 °C, 0.70 °C, 1.06 °C respectively). The calibration results indicate the Pr probe method to be most sensitive and accurate. However, this advantage could only be partially transferred to the thermographic maps because of the coarse 16×16 matrix of the classical CSI sequence. Therefore, at present the water PRF method appears to be most suitable for MR monitoring of small temperature changes during hyperthermia treatment.

1. Introduction

Further progress in radiofrequency regional hyperthermia of deep-seated (for example pelvic) tumours depends on the development of a non-invasive control of temperature distributions in the patient (Wust *et al* 1995). It is hoped that this non-invasive thermography will accomplish two tasks in a future scenario of hyperthermia treatments for pelvic tumours: localization and surveillance. During localization the temperature monitoring should detect undesired hot spots induced at dielectric discontinuities of pelvic tissue (muscle, fat and bone) so that they can be resolved by appropriately steering the power deposition pattern (Wust *et al* 1996).

§ Address for correspondence: Strahlenklinik und Poliklinik, Charité Medical School—Campus Virchow-Klinikum, Augustenburger Platz 1, 13353 Berlin, Germany. E-mail address: waldemar.wlodarczyk@charite.de

0031-9155/99/020607+18$19.50

After a proper power distribution is adjusted, temperature monitoring is required to survey the achieved temperature distributions in tumour and neighbouring normal tissue, indicating possible depressions to be corrected via the applicator steering parameters.

Recently, several magnetic resonance (MR) thermography methods have been reported as promising candidates for non-invasive temperature control. They can be classified according to the utilization of endogeneous or exogeneous temperature indicators. The endogeneous temperature indicators are spin–lattice relaxation time T_1 (Parker *et al* 1983, Dickinson *et al* 1986), self-diffusion coefficient D (Le Bihan *et al* 1989) and shift of the water proton resonance frequency (water PRF) (Hall and Talagala 1985, Ishihara *et al* 1995). Chemical shift can be exploited as an exogeneous temperature indicator and is associated with compounds such as cobalt (Webb *et al* 1993) or lanthanide chelates (Bleaney 1972), particularly ytterbium (Aime *et al* 1996), thulium (Zuo *et al* 1996) and praseodymium (Konstanczak *et al* 1995, Frenzel *et al* 1996, Hentschel *et al* 1998a). Although some of these methods have already been successfully applied for monitoring high-temperature elevations (near 80 °C) associated with thermoablative interventions (for example Vogl *et al* 1995, Cline *et al* 1994, 1996), they cannot be directly adopted for monitoring small temperature changes during hyperthermia treatments. The specific demands for temperature monitoring during hyperthermia differ considerably from those applied during thermoablative interventions. Normally, the temperatures to be monitored do not exceed 43 °C (maximum 45 °C). During the localization phase of hyperthermia treatment fast volume scans of the entire pelvis have higher priority and, therefore, moderate thermal and spatial resolution can be accepted (Wlodarczyk *et al* 1998a, b). During the surveillance phase of hyperthermia treatment, temperature monitoring can be limited to the tumour and its neighbourhood. Consequently, acquisition of only one or few slices is sufficient. Here, the temperature accuracy desired would be better than 1 °C (Cetas 1984).

The purpose of this work was a systematic comparison of the four MR thermography methods (T_1, D, water PRF and Pr probe) in phantom experiments with regard to their planned application for monitoring hyperthermia treatments. The criterion of this comparison was the thermal resolution achieved under the constraint of the total acquisition time fixed to a value of approximately 4 min at a clinical scanner with a standard gradient hardware. For this, four different pulse sequences, which are associated with the four MR thermography methods, were optimized for the particular phantom in order to achieve the highest thermal resolution possible. For an exact verification in the presence of spatial temperature gradients high planar resolution was necessary. In order to simulate a possible scenario of hyperthermia monitoring, experiments consisted of two parts: calibration and mapping.

2. Materials and methods

2.1. MR thermography methods

2.1.1. Spin–lattice relaxation time T_1. The relationship between T_1 and small temperature variations was found to be approximately linear with sensitivities of 0.8% $^\circ C^{-1}$ to 2% $^\circ C^{-1}$ (Parker *et al* 1983, Parker 1984, Dickinson *et al* 1986, Hall *et al* 1990). The quality of T_1 based MR thermography depends on the accuracy with which T_1 itself can be determined. The latter constitutes the actual difficulty of the method. Conventional methods, which determine T_1 by fitting a recovery curve to a series of measurements, such as the multipoint inversion recovery (IR) or the repeated saturation recovery (SR) methods, are the most accurate but also the most time-consuming approaches (Crawley and Henkelman 1988). Methods based on only few measurements, such as the spin echo (SE) with two different repetition times (T_R) or the

gradient echo (GE) with different flip angles, produce inaccurate T_1 estimates (for example Prato *et al* 1986). The recently reported rapid T_1 mapping techniques, known as 'snapshot' or 'turboflash' significantly speed up the acquisition process, but they either suffer from a large uncertainty of measured T_1 (Haase 1990) or need excessive post-processing (Tong and Prato 1994). Improving the accuracy of T_1 for these methods again requires a greater number of measurements (Blüml *et al* 1993). T_1 measurements using echo-planar imaging require fast gradient hardware (Gowland and Mansfield 1993). Also pulse sequences with strongly T_1 weighted gradient echo have been occasionally applied for fast temperature monitoring, especially in MR guided thermoablative interventions with high temperature elevations (for example Matsumoto *et al* 1994). These methods are neither sensitive nor accurate enough for monitoring small temperature changes during hyperthermia treatments (Wlodarczyk *et al* 1998a). With its potential to combine high accuracy and moderate acquisition times, we implemented an imaging version of the spectroscopic Look and Locker technique (Look and Locker 1970) as a T_1 based MR thermography method. The method known as TOMROP (T One by Multiple Read Out Pulses) applies an inversion pulse followed by a train of evenly spaced interrogation pulses of small flip angle (Graumann *et al* 1986, Brix *et al* 1990).

2.1.2. Self-diffusion coefficient D. A linear relationship between diffusion coefficient D and temperature (via thermal Brownian motion) is given by the Stokes–Einstein relation. In the physiological temperature range the thermal sensitivity of diffusion is approximately $2.4\%\,^{\circ}\mathrm{C}^{-1}$ (Zhang *et al* 1992). Nearly each MR pulse sequence can be sensitized for diffusion by a pair of magnetic field gradient pulses (Stejskal and Tanner 1965), which cause a phase offset in spins randomly moving in a direction along these gradients. The attenuation of the echo signal can then be expressed by

$$S = S_0\,\mathrm{e}^{-bD} \tag{1}$$

where S_0 is the signal in the absence of diffusion gradients and b is a factor for diffusion sensitization. For square diffusion gradients b can be calculated by

$$b = (\gamma G\delta)^2(\Delta - \delta/3) \tag{2}$$

where G is the strength, δ the duration and Δ the separation of the diffusion gradient pulses. An accurate multipoint fit of D requires several acquisitions of the same pulse sequence with several b values. Unfortunately, this prolongs excessively the total acquisition time. Accurate and fast D based thermography is possible when using echo planar imaging, but this requires fast gradient hardware (MacFall *et al* 1995, Il'yasov and Hennig 1997). The conventional pulsed gradient spin echo (PGSE) sequence without ($b_1 = 0$) and with one pair of diffusion gradients ($b_2 \neq 0$; two-point technique) in all three axes was applied in this study.

2.1.3. Water proton resonance frequency (PRF) shift. With increasing temperature the screening effect of bounded electrons increases, resulting in a lower local magnetic field and, consequently, in a negative shift of water PRF, which has been reported to be $-0.0107\,\mathrm{ppm}\,^{\circ}\mathrm{C}^{-1}$ in pure water (Hindman 1966, Lutz *et al* 1993) and in the range between -0.007 and $-0.009\,\mathrm{ppm}\,^{\circ}\mathrm{C}^{-1}$ in muscle and other organ tissues with a linear relationship up to $50\,^{\circ}\mathrm{C}$ (Kuroda *et al* 1993). The temperature induced shift of water PRF is usually extracted from phase difference of two gradient echoes (Ishihara *et al* 1995). Phase images are acquired before and after heating and subtracted to obtain phase difference images, which are proportional to the temperature-dependent shift of water PRF.

For temperature measurements, all other sources of phase changes such as magnetic susceptibility or magnetic field drifts must be eliminated. Then the temperature-dependent

phase difference can be written as

$$\Delta\varphi/\Delta T = \gamma B_0 \delta(T) T_E \tag{3}$$

where $\gamma/2\pi = 42.58$ MHz T^{-1} is the gyromagnetic ratio of hydrogen, B_0 is the flux density of the main magnetic field, $\delta(T)$ is the temperature-dependent shift of water PRF in ppm $^\circ$C^{-1}, and T_E is the echo time for the phase accumulation. In this work the fast low angle shot (FLASH) sequence (spoiled gradient echo) was employed for measurement of temperature induced water PRF shift.

2.1.4. Praseodymium temperature probe. Recently, the complex of praseodymium-2-methoxyethyl-DO3A (Pr-MOE-DO3A) has been investigated as an exogeneous temperature indicator (Pr probe) applying ^{1}H MR spectroscopy (MRS) (Frenzel *et al* 1996, Hentschel *et al* 1998a). Like other lanthanides, when exposed to varying temperatures Pr strongly influences the ^{1}H MR spectrum. Compared with gadolinium as a central atom of MR contrast media, Pr is only weakly paramagnetic and, therefore, more suitable as a basis for synthesis of temperature indicators. The temperature-dependent functional group of the Pr probe is the methoxy group (OCH3) with thermal sensitivity of 0.12–0.13 ppm $^\circ$C^{-1}. For spatial encoding of the temperature information 2D classical chemical shift imaging (CSI) was applied.

2.2. Experimental set-up and instrumentation

All experiments employed a cylindrical phantom made of lucite with two concentric walls (inner and outer diameter of 11 and 14 cm respectively) and a double bottom (inner and outer height of 12.5 and 14 cm respectively). The inner cylinder was homogeneously filled with agarose gel laced with 2.5 mM gadolinium-DTPA for matching relaxation properties of muscle tissue. In addition, 9.5 mM Pr-MOE-DO3A complex was admixed. Four parallel fibres with fluoroptic temperature sensors with $\pm 0.2\,^\circ$C accuracy (Luxtron MPM, Mountain View, CA, USA) were axially inserted reaching down half the cylinder depth. This MR compatible thermometry system is based on the temperature dependence of the luminescent decay time (associated with fluorescent afterglow). The sensitive luminescent element is attached to an optical fibre and excited via a filtered xenon flash lamp with light pulses that are of microsecond duration. The luminescent decay time is in the millisecond range. Thus, excitation and emission are well separated in the time domain. Detection is performed using a photodiode. In order to measure and correct for drifts of the static magnetic field four thermally isolated cylindrical agarose gel reference phantoms with 3 cm diameter were placed outside the main phantom. Water circulating in the double wall of the cylinder and thermally regulated via a thermostat (E8-46, Haake Messtechnik GmbH, Karlsruhe, Germany) provided the desired temperature distribution. All MR thermography experiments were performed in a 1.5 T clinical whole-body scanner (Magnetom 63 SP, Siemens AG, Erlangen, Germany) equipped with standard gradient hardware providing a gradient strength of 10 mT m^{-1} and a gradient slew rate of 10 mT m^{-1} ms^{-1}. Transmitting and receiving was performed by a circularly polarized head coil.

2.3. Material properties of the phantom

Standard methods with long acquisition times (Wlodarczyk *et al* 1998a) allowed a quite accurate determination and mapping of the phantom's properties such as spin–lattice relaxation time T_1, true and apparent spin–spin relaxation times T_2 and T_2^* and self-diffusion coefficient D. The measured relaxation or diffusion data were fitted on a pixel-by-pixel basis to corresponding

Table 1. Material properties measured in the homogeneous central and lower parts of the phantom.

Properties of the phantom material	Measured value
Spin–lattice relaxation time T_1	532 ± 35 ms
Spin–spin relaxation time T_2	59 ± 11 ms
Effective spin–spin relaxation time T_2^*	41 ± 7 ms
Self-diffusion coefficient D	$1.94 \pm 0.17\ 10^{-3}$ mm^2 s^{-1}

exponential curves employing the Levenberg–Marquardt algorithm (Press *et al* 1992). Then, maps of the desired MR parameters were generated. Only material values obtained from the homogeneous central and lower parts of the phantom were recruited as a basis for the optimization of pulse sequences (table 1).

2.4. Optimization of pulse sequences

For an efficient application of the four MR thermography methods, four different pulse sequences were optimized. The aim of the optimization was the highest thermal resolution for the particular phantom material in consideration of some general and sequence-specific constraints. The general constraints are the gradient strength of 10 mT m^{-1} and the slew rate of 10 mT m^{-1} ms^{-1}, a fixed total acquisition time of approximately 4 min and a planar resolution as high as possible (but not higher than 256^2) in order to resolve the spatial temperature gradients with regard to the verifying fluoroptic thermometers. The sequence-specific constraints are presented in corresponding sections below. The rather long total acquisition time of 4 min was due to the slow CSI sequence, which at that time could be only acquired with a coarse matrix of 16×16 and corresponding pixel size of 11.2×11.2 mm^2 (for the field-of-view of 180 mm^2). For the three tomographic sequences an equal number of frequency encoding samples of $N_{\mathrm{fr}} = 256$ was applied. This high resolution was achieved in the phase encoding direction ($N_{\mathrm{ph}} = 256$) only with the FLASH sequence, whereas with the TOMROP sequence $N_{\mathrm{ph}} = 196$ and with the PGSE sequence $N_{\mathrm{ph}} = 128$ could only be obtained. The respective pixel size values were 0.9×0.9 mm^2, 0.9×1.8 mm^2 and 0.9×1.2 mm^2 (for the field of view of 230 mm^2). The tomographic pulse sequences were applied with a larger field of view than the CSI, because the reference phantoms for tracking field drift had to be contained (at least for water PRF). All measurements referred to an equal slice thickness of 10 mm chosen in-plane with the fibre array of the fluoroptic thermometer system.

2.4.1. TOMROP. An usual way to optimize the TOMROP sequence is the search for optimal values of the time interval τ and the flip angle α of the interrogative pulses. But in order to get as many phase encodings as possible our first objective was to shorten T_R as much as tolerable. Shortening T_R shortens the time for recovery and the systematic error of the deduced T_1 increases, but at $T_R = 1200$ ms($\approx 2T_1$) it seems still to be sufficiently low when interrogation pulses with small flip angle ($\alpha = 17^\circ$) are applied (Kay and Henkelman 1991). For the total acquisition time of approximately 4 min it results in 196 phase encodings. In order to reduce the random errors, the time interval τ should usually be optimized, but we no longer did that after we found that the random errors were mostly affected during the numerical fitting. In order to get a sufficient number of sample points for robust numerical fitting to run automatically pixel-by-pixel, we decided to use a large number of interrogative pulses ($N = 32$). In order to get good estimates of T_1, we again followed suggestions of Kay and Henkelman (1991) and spaced the interrogative pulses equally across T_R. On the other hand, after choosing

values for T_R and N as given above there remains little room to vary τ in a way which has a non-negligible effect upon the signal-to-noise ratio (SNR). In order to further improve the accuracy and the reliability of the T_1 based temperature measurements some modifications to the original TOMROP pulse sequence were introduced. Spoiler gradients after each gradient echo destroyed any residual transverse magnetization. A hyperbolic secant inversion pulse with double bandwidth of interrogating pulses improved slice selectivity (Gowland and Leach 1992). Each series of 32 signal intensities

$$S_i = a(1 - c\,\mathrm{e}^{-\mathrm{i}\tau/T_1^*}) \tag{4}$$

was fitted with three parameters (T_1^*, a, c), eventually giving T_1 via $T_1^* = \tau/(\tau/T_1 - \ln\cos\alpha)$.

2.4.2. PGSE. In general, in order to get a good estimation of D, more b images should be acquired (multipoint technique). However, this prolongs extensively the total acquisition time. On the other hand, it has been shown that a two-point technique is sufficient when an optimal set of gradient pairs is used (for example Zhang *et al* 1992). Applying the two-point technique with $b_1 = 0$, the only sequence parameter which can be optimized with regard to the phantom properties is T_E. In order to get a reasonable diffusion attenuation, δ, and consequently T_E, should be large. In addition, δ should be as close as possible to Δ. On the other hand, T_E has to be short enough to maintain a reasonable SNR under T_2 relaxation. The optimization of T_E was performed with noise sensitivity D as the objective function and with consideration of the phantom properties. The optimal values were found to be $T_E = 120$ ms, $\Delta = 55$ ms and $\delta = 39$ ms. Keeping in mind the total acquisition time of approximately 4 min, there remain only three parameters to be optimized: T_R, N_{ph} and number of acquisitions. These remaining parameters were chosen with regard to the SNR in an experimental way. Considering that the total acquisition time means the sum of acquisition times of both b images required for generation of one D image, we decided to apply $T_R = 940$ ms, $N_{\mathrm{ph}} = 128$ and one acquisition for both parts of the PGSE (i.e. 2×2 min).

2.4.3. FLASH. For the FLASH pulse sequence the quotient of accumulated phase differences $\Delta\varphi$ and standard deviation of the phase difference image $\sigma_{\Delta\varphi}$, $\mathrm{SNR}_{\Delta\varphi} = |\Delta\varphi|/\sigma_{\Delta\varphi}$, was optimized towards its maximum. The objective function depending on the material properties of the phantom and the acquisition time then reads

$$\mathrm{SNR}_{\Delta\varphi} \propto |\Delta\varphi S_{\mathrm{FLASH}}| = |\gamma B_0\,\delta(T)\Delta T|\rho M_0 \frac{\mathrm{e}^{-T_E/T_2^*}(1 - \mathrm{e}^{-T_R/T_1})\sin\alpha}{1 - \mathrm{e}^{-T_R/T_1}\cos\alpha} \tag{5}$$

where S_{FLASH} is the magnitude signal, ρ the proton density and M_0 the equilibrium magnetization. The phase difference $\Delta\varphi$ accumulating during echo time enhances $\mathrm{SNR}_{\Delta\varphi}$ with longer T_E (first factor in equation (5)). On the other hand, as can be concluded from noise considerations of MRI data (Pelc *et al* 1991, Gubdjartsson and Patz 1995), $\sigma_{\Delta\varphi}$ is inversely proportional to the magnitude signal, resulting in direct proportionality of the $\mathrm{SNR}_{\Delta\varphi}$ to S_{FLASH} (second factor in equation (5)). Conversely to $\Delta\varphi$, S_{FLASH} decreases with T_E due to T_2^* relaxation. Thus, an optimal T_E value resulting in maximal $\mathrm{SNR}_{\Delta\varphi}$ exists for every T_2^* value. In addition, $\mathrm{SNR}_{\Delta\varphi}$ can be further increased employing longer T_R and an optimal flip angle α. Assuming phantom material properties, the maximum $\mathrm{SNR}_{\Delta\varphi}$ was achieved for $T_E = 60$ ms and $\alpha = 60^\circ$, the latter corresponding to the Ernst angle (Ernst and Anderson 1966). This theoretical optimization of the temperature sensitivity of spoiled gradient echo has been experimentally verified by Chung *et al* (1996). Assuming the total acquisition time of 4 min, $T_R = 240$ ms and four excitations, 256 phase encoding lines were acquired.

2.4.4. MRS and classical 2D CSI. For the purpose of Pr based MR thermography, a classical 2D CSI pulse sequence with phase encodings in both orthogonal directions and acquisition of the free induction decay (Maudsley *et al* 1979) was modified for slice selective (10 mm) off-resonance (−24 ppm) excitation with a planar matrix of 16 × 16. The CSI pulse sequence was optimized experimentally. The objective was SNR maximization of the methoxy spectral line. In order to avoid an extensive analysis of ^{1}H spectra after each CSI optimization step, this optimization was performed in equivalent MRS experiments employing menu guided standard MRS analysis software of the scanner. Off-resonance excitation with Gaussian shaped 250 Hz rf pulses reduced the unwanted water signal. For signal detection a vector size of 256 sample points with 1 ms dwell time was selected, resulting in $T_R = 275$ ms and a spectral width of ±500 Hz. The low-pass filter of the receiver was adapted to the latter. The receiver gain was maximized. Artefacts and noise were reduced applying four prescans and four acquisitions. The thus optimized MRS pulse sequence was utilized in calibration experiments. It was also the basic element of the CSI pulse sequence. $T_R = 275$ ms and the matrix of 16 × 16 phase encodings determined the total acquisition time of 250 s per CSI pulse sequence.

2.5. Calibration and mapping experiments

The experiments were done in two separate and consecutive steps performed on different days but under identical experimental conditions. In the first step, only calibration curves were recorded. These curves were used to calibrate temperature induced changes of MR parameters measured during the second step and to generate maps of temperature changes. At the beginning of each step the phantom was thermally equilibrated by peripherally circulating water at 35 °C. After turning off the water circulation (to avoid flow artefacts), measurements employing all four MR thermography methods were consecutively performed. Then, the phantom was further heated by circulating water, this time at 45 °C, generating radial temperature gradients with a minimum temperature in the phantom centre. Again, water circulation was turned off during MR measurements. This procedure was repeated six times with the first series taken as reference. Real temperature measured fluoroptically in the middle of each acquisition was taken for verification. At this time, the contrast-determining central lines of the k-space were acquired. For the purpose of controlling possible temporal changes of temperature during the acquisition, real temperature was also picked up at the beginning and at the end of each acquisition.

After measurements of the calibration step, maps of temperature-dependent MR parameters, P_{MR}, were generated applying method-specific post-processing (see section 2.6). Then, maps of fractional changes of the temperature-dependent MR parameter, ΔP_{MR}, were generated. We derived the calibration curves for the tomographic methods from mean values of four equal regions of interest (approximately 10 mm^2) positioned at an axial distance of 4 mm from the tips of the fluoroptic sensors. This small distance should avoid susceptibility errors caused by insertion of the sensors, especially affecting the temperature measured by the water PRF method (DePoorter 1995). ΔP_{MR} were plotted against real temperature changes ΔT_{FL}. Calibration curves were derived from scatter plots by linear regression employing a single-parameter model ($\Delta P_{\mathrm{MR}} = m_{\mathrm{CAL}} \Delta T_{\mathrm{FL}}$). The quality of linear regression is described by the coefficient of determination r^2_{CAL} as well as the mean value and the standard error of slope $m_{\mathrm{CAL}}(\pm\sigma_m)$ which is the temperature sensitivity. An analysis of residuals applied to the inverted scatter data yielded the standard error $\sigma_{\Delta T}$ and, thus, the uncertainty of predicting temperature changes from changes of corresponding temperature-dependent MR parameters.

Data measured in the second step were processed in a similar way and calibrated by curves from the calibration experiments to deliver maps of temperature changes ΔT_{MR}. These

maps were verified by fluoroptic measurements of real temperature changes ΔT_{FL}. A linear regression analysis, now based on the two-parameter model ($\Delta T_{MR} = m_{MAP}\Delta T_{FL} + b_{MAP}$) yielded the correlation coefficient r_{MAP}, mean values and standard errors of both the slope m_{MAP} ($\pm\sigma_m$) and the intercept b_{MAP} ($\pm\sigma_b$). The systematic error and the uncertainty of the temperature changes extracted from those maps are given by the mean deviation MD and the root mean square deviation RMSD, respectively.

2.6. Image processing

The TOMROP data were fitted on a pixel-by-pixel basis using the Levenberg–Marquardt algorithm (Press *et al* 1992). Robustness of operator-free fitting was increased by such measures as a large number of sampling points ($N = 32$), start and limiting parameters based on expected values and tracking of errors. However, not all pixels were successfully fitted to realistic T_1 values, which is a typical phenomenon of automatic procedures. The faulty fits were detected and classified during the numerical procedure. Since most misfitted pixels were surrounded by well fitted regions, missing values were interpolated from T_1 values of neighbouring pixels. Maps of fractional T_1 changes were obtained comparing the reference and the successive T_1 maps. From the maps of fractional T_1 changes maps of temperature changes were generated using the calibration data. Unfortunately, these maps were still too noisy to generate isotherms and therefore a 2D median filter averaging over five pixels was applied. Finally, smooth temperature maps were obtained and isotherms of 0.5 °C were overlaid.

Maps of D were deduced from the ratio of the two SE images (equation (1)), one acquired without and the other with diffusion gradients. Again, maps of fractional D changes and, after calibration, maps of temperature changes were generated, which were smoothed and overlaid by isotherms in the way described above.

Both magnitude and phase FLASH images (complex images) were used to generate $\Delta\varphi$ maps associated with temperature-dependent water PRF shift. The gradient correction, usually applied with phase image reconstruction, was turned off. Multiplying the reference complex image acquired before heating with conjugate complex images acquired during heating gave the $\Delta\varphi$ maps (Chung *et al* 1996). This complex image subtraction avoids phase wrapping due to the encoding scheme and inhomogeneities and was, therefore, preferred over the simple phase image subtraction. However, $\Delta\varphi$ might also exceed $\pm\pi$ due to large temperature changes and/or drifts of the static magnetic field. Therefore, a simple (manual) phase unwrapping scheme was still to be applied. Phase difference changes due to drifts of the static magnetic field were $3(\pm1)^\circ\ h^{-1}$ during the calibration experiments and $7(\pm2)^\circ\ h^{-1}$ during the mapping experiments. These drifts were corrected utilizing external reference phantoms (De Poorter *et al* 1994). In comparison with maps of fractional T_1 and D changes, the maps of $\Delta\varphi$ were less noisy but superimposed with susceptibility artefacts which mimic non-existent hot spots. These artefacts were recognized as extremely high gradients of $\Delta\varphi$, the respective pixels were marked and their values replaced by values interpolated again using the adjacent pixels. These procedures were particularly necessary in the upper inhomogeneous parts of the phantom and outside the phantom material, although the latter could also be masked out. Again, maps of temperature changes were generated, which were smoothed and overlaid by isotherms in the way described above.

Spectra of every CSI experiment were fused with a spin–echo image of the same field of view. While the analysis of MRS data employed menu guided the scanner software, CSI data was analysed off-line using commercially available software (Igor Pro 3.01, Wave Metrics Inc., Lake Oswego, OR, USA). Each spectrum was manually processed. First, the FID was

zero-filled doubling the sampling points and apodized, multiplying with an exponential of 5 Hz linewidth to improve the SNR. Then, a fast Fourier transform was performed and the subsequent processing steps were carried out in the frequency domain including zero-order phase correction and peak position determination of the methoxy group by least-square Lorentzian line fitting. The chemical shift of the methoxy group relative to the position at the equilibrium (before heating) was the parameter used for calibration and for generation of maps of temperature changes. The same software was applied to render isotherms as contour plots.

3. Results

3.1. Calibration curves

Figure 1 shows scatter plots from calibration experiments for all four MR thermography methods. The linear temperature dependence of MR parameters proves the theoretical models to be correct in the specified temperature range. A strong dependence of the statistical fluctuations on the method is evident. Deviation of measured data from regression lines increases slightly at higher temperature gradients. These errors are predominantly caused by averaging high spatial temperature gradients. Table 2 summarizes the regression analysis results of calibration data. The best linearity of MR parameter changes ΔP_{MR} versus fluoroptic temperature changes ΔT_{FL} (represented by the coefficient of determination r^2_{CAL}) in conjunction with the lowest uncertainty of temperature prediction (represented by the standard error of the inverted scatter plot $\sigma_{\Delta T}$) was obtained applying the Pr probe in the MRS experiments. For the tomographic methods, the best results were obtained using the water PRF shift followed by the D and the T_1 based methods. For all four MR thermography methods the uncertainty of temperature prediction from calibration curves was less than 1 °C.

Table 2. Results of linear regression analysis of calibration experiments in a homogeneous phantom for all four MR thermography methods. The analysis was based on a one-parameter model ($\Delta P_{MR} = m_{CAL}\Delta T_{FL}$). The number of measured data points was $n = 20$.

Parameters of linear regression analysis	T_1	D	Water PRF	Pr probe
Coefficient of determination r^2_{CAL}	0.915	0.981	0.995	0.999
Slope of the regression line (temperature sensitivity) m_{CAL}	$1.60 \pm 0.05\%\,^\circ C^{-1}$	$2.21 \pm 0.04\%\,^\circ C^{-1}$	$12.6 \pm 0.2^\circ\,^\circ C^{-1}$	0.128 ± 0.001 ppm $^\circ C^{-1}$
Standard error of inverted plot (uncertainty) $\sigma_{\Delta T}$	0.93 °C	0.48 °C	0.22 °C	0.11 °C

3.2. Maps of temperature changes

For the three tomographic methods maps, of temperature changes based on the calibration curves (m_{CAL}) were generated for the central transverse cross section of the phantom (figure 2). Those were superimposed with contour plots of 0.5 °C isotherms of relative temperature changes. For Pr based thermography, contour plots of 1 °C isotherms of absolute temperature were rendered (figure 3). These maps cannot be quantitatively compared because they were acquired during the dynamic process of heating. However, a qualitative similarity of temperature distribution can be observed. The slight asymmetry of temperature distribution is probably caused by an asymmetrical arrangement of the fibreoptic sensor array with respect to the phantom axis.

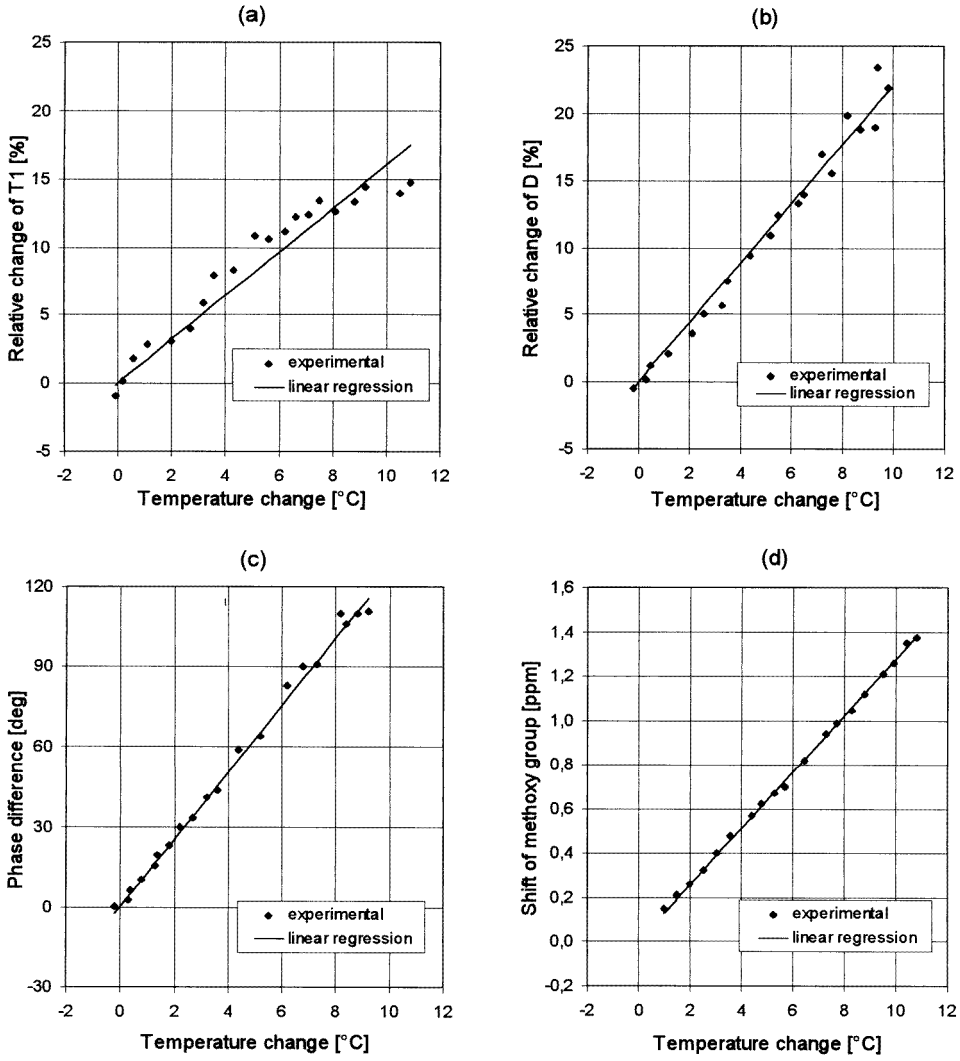

Figure 1. Scatter plots and regression lines showing the linear dependence between fractional changes of the four MR specific temperature indicators and temperature changes measured fluoroptically (calibration experiments): T_1 (*a*), D (*b*), water PRF (*c*) and Pr probe (*d*). The linear regression analysis was based on a one-parameter model.

3.3. Verification of temperature maps

The verification of temperature maps was performed by comparing MR measured temperature changes ΔT_{MR} with directly (fluoroptically) measured temperature changes ΔT_{FL}. Figure 4 shows the correlation between ΔT_{MR} and ΔT_{FL} in scatter plots. For all four methods the linearity still holds. However, due to error propagation the deviation of measured data from regression lines is higher than in the calibration experiments. Errors in the tomographic experiments are now not predominantly caused by averaging high spatial temperature gradients. Rather, there are various error sources which cause deviations uniformly distributed over the whole temperature range.

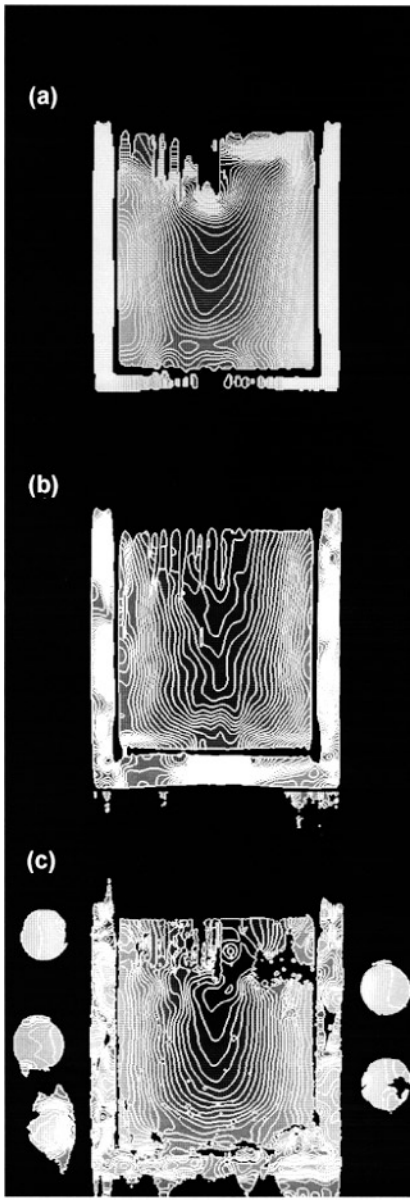

Figure 2. Maps of temperature changes with 0.5 °C isotherms obtained applying methods of T_1 (*a*), D (*b*) and water PRF based MR thermography (*c*) in the central transverse slice of the phantom.

Table 3 summarizes results of the regression analysis regarding the mapping experiments. In the case of the CSI experiment, spatial averaging increases errors due to the coarse matrix 16×16). The most favourable results quantified by the correlation coefficient r_{MAP} and the root mean squared deviation, RMSD, were achieved using the water PRF method, followed by D and T_1 based methods. The uncertainty of ΔT_{MR} indicated by the RMSD is considerably higher than $\sigma_{\Delta T}$ in the calibration experiments but remains below or near the required limit of

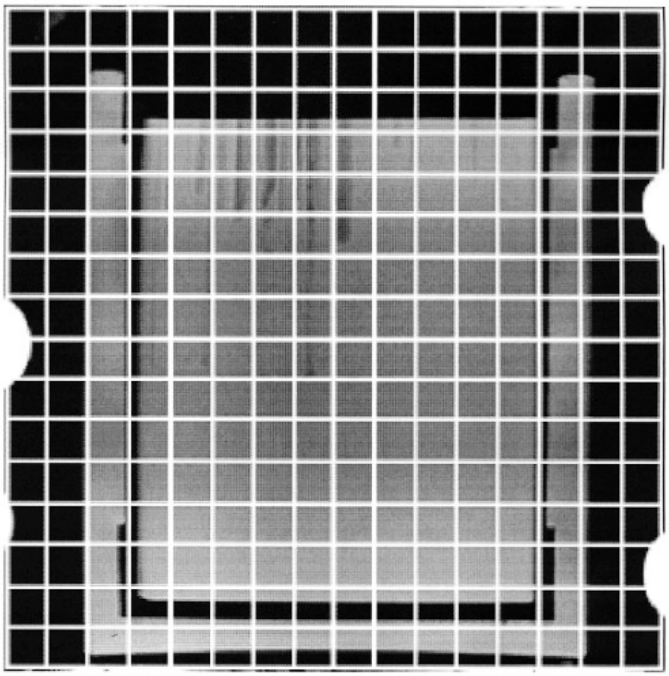

(*a*)

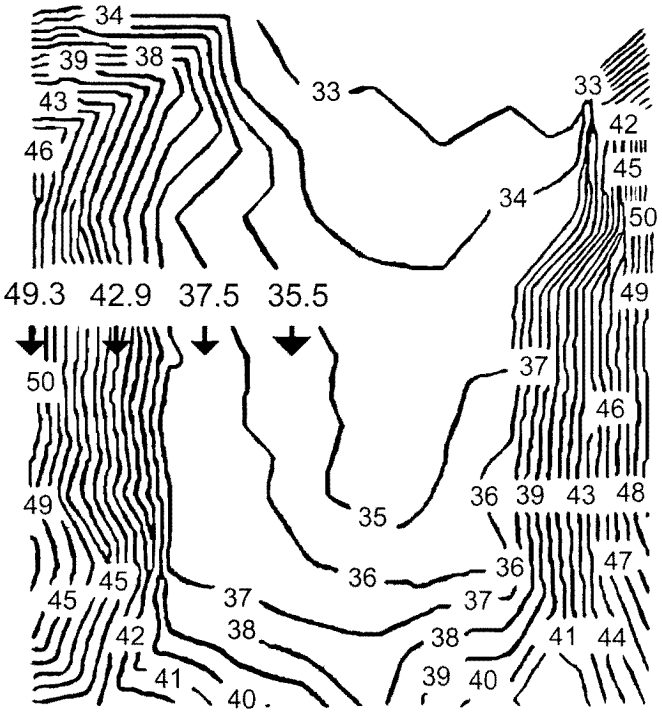

(*b*)

Figure 3. Spin echo image of the central transverse slice of the phantom superimposed with the CSI grid (*a*) and contour plot of 1 °C isotherms obtained by the Pr based MR thermography method (*b*).

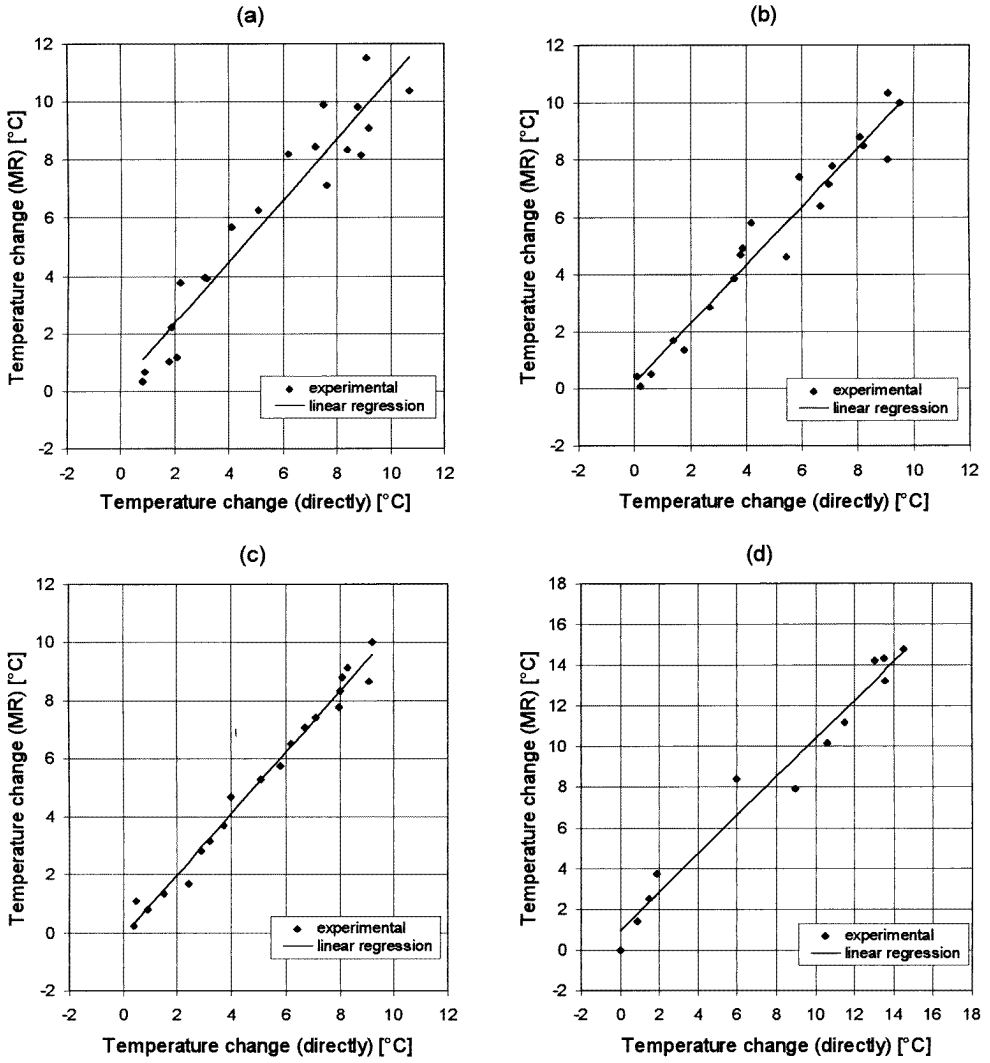

Figure 4. Scatter plots and regression lines showing the correlation between temperature changes measured applying the four MR thermography methods and temperature changes measured fluoroptically (mapping experiments): T_1 (*a*), D (*b*), water PRF (*c*) and Pr probe (*d*). The linear regression analysis was based on a two-parameter model.

1 °C for all four MR thermography methods. Thus, the temperature resolution of 1 °C desired for clinical use is achieved with all four MR thermography methods.

4. Discussion

To our knowledge, a systematic comparison of MR thermography methods with regard to their thermal resolution and under approximately identical experimental conditions has only been presented in parts. There exists a theoretical and experimental comparison of different T_1 based thermography methods (Le Roux and Saint-Jalmes 1993). Furthermore, methods

Table 3. Results of linear regression analysis of mapping experiments in a homogeneous phantom for all four MR thermography methods. The analysis was based on a two-parameter model ($\Delta T_{MR} = m_{MAP}\Delta T_{FL} + b_{MAP}$). The number of measured data points was $n = 20$ for the T_1, D and water PRF methods, and $n = 12$ for the Pr probe method.

Parameters of linear regression analysis	T_1	D	Water PRF	Pr probe
Correlation coefficient r_{MAP}	0.955	0.976	0.992	0.984
Slope of regression line m_{MAP}	1.06 ± 0.08	1.02 ± 0.05	1.05 ± 0.03	0.95 ± 0.05
Intercept of regression line b_{MAP}	0.23 ± 0.49	0.23 ± 0.31	-0.10 ± 0.18	0.92 ± 0.52
Mean deviation MD	$-0.56\,^{\circ}$C	$-0.33\,^{\circ}$C	$-0.16\,^{\circ}$C	$-0.48\,^{\circ}$C
Root mean square deviation RMSD	$1.06\,^{\circ}$C	$0.70\,^{\circ}$C	$0.41\,^{\circ}$C	$0.97\,^{\circ}$C

utilizing two different MR temperature indicators, such as D and water PRF, have been experimentally compared, postulating superiority of the latter (De Poorter *et al* 1994). A theoretical comparison of the D based method with a two-point T_1 measurement predicted superiority of the T_1 method (Saint-Jalmes 1995).

The comparison of the four MR thermography methods presented in this study was carried out with regard to their feasibility for monitoring regional rf hyperthermia treatments in the pelvis. This lead to the specific experimental set-up and measurement scenario. Thus the main emphasis has been put on the spatial temperature gradients which are of particular importance in rf hyperthermia in the pelvis. Such hyperthermia treatments are impaired by regional parasitic hot spots which are induced by dielectric discontinuities (muscle, fat and bone) of pelvic tissue. The temporal temperature gradients are negligible because, in contrary to the thermoablative interventions, the hyperthermic heating is a relatively slow process. These specific conditions have been taken into account when planning the experiments with circulating and slowly warming water as a heat source. The total duration of each experiment series of approximately 2 h corresponds to the maximum treatment time. In general, the temperature changes during common MR acquisition times are very low. The largest differences between temperature values measured fluoroptically at the beginning and at the end of the acquisitions were less than $\pm 0.2\,^{\circ}$C. In order to avoid even these remaining temporal effects, thermal equilibrium should be obtained before each temperature measurement. Using our experimental set-up, this would prolong the duration of the entire experiment for far longer than the duration of hyperthermia treatments, giving rise to more problems with instabilities of the MR tomograph (De Poorter *et al* 1995).

In future clinical applications for monitoring hyperthermia treatments the MR thermography methods should first be calibrated in order to get calibration data for on-line temperature monitoring. This is especially necessary when a T_1 based method is intended to be used, because T_1 and its temperature induced changes are tissue dependent. For the water PRF method calibration is useful to better discriminate between muscle and fat tissue. The reason for the calibration of the D method is the dependence of the activation energy on the tissue structure. Performing calibration and mapping experiments on different days, i.e. repositioning and reheating the phantom in between them, should approach this intended scenario. In this way, we added to the original statistical errors other uncertainties due to error propagation.

The calibration experiments provided accuracies for prediction of temperature changes

from MR indicator changes to be better than 1 °C. The accuracy of thermometry based on the Pr probe using MRS (±0.11 °C) proved even to be on the scale of the fluoroptic thermometer. The order of other methods with regard to accuracy was: water PRF, D and T_1. In the mapping experiments, the three thermographic methods showed only slightly reduced temperature resolution compared with the calibration results. Still being better than or around 1 °C, the highest temperature resolution was now achieved with the water PRF method (±0.4 °C) followed, as above, by D and T_1 methods. Unfortunately, the Pr probe approach was here hampered by a coarse matrix resulting in errors from averaging over spatial temperature gradients. Nevertheless, the potential of the Pr probe as an exogeneous temperature indicator has been clearly demonstrated in the calibration experiment. This potential can be exploited when faster CSI sequences are applied, allowing higher planar resolution to be obtained without prolongation of the acquisition time (Hentschel *et al* 1998b, Noeske *et al* 1998).

These promising results were achieved with relatively long acquisition times of approximately 4 min and relatively high planar resolution (at least for tomographic methods). The rather long total acquisition time was due to the slow CSI sequence. The high planar resolution was necessary for the phantom experiments in order to avoid averaging errors when verifying the MR thermography by fluoroptic thermometers. Although, the planar resolution was not exactly equal, it was on the same scale (128–256 × 256) at least for the tomographic sequences. Unfortunately, only a very low planar resolution of 16 × 16 was obtained by applying the CSI sequence. This planar resolution is too low to resolve spatial temperature gradients and results in considerable averaging errors in mapping experiments. It is true that it would be desirable for the purpose of a consistent comparison to apply equal spatial resolution for all sequences. Unfortunately, such comparison between the tomographic and CSI sequences was not possible with the available equipment. On the other hand, if we restricted this comparison only to the tomographic sequences, it would be possible to reduce the image matrices of all sequences to the common denominator, i.e. to the coarsest matrix of 128 × 256, and hold constant the total acquisition time constant by appropriate averaging or adjusting T_R. However, we decided to get the largest planar resolution possible for every sequence. Thus different numbers of phase encodings resulted in different planar voxel dimensions and so in different SNR conditions. However, these different SNR conditions have been equalized during quantitative evaluation by holding constant the actual areas of the specified regions of interest (approximately 10 mm^2). On the other hand, the qualitative analysis resulting in plots of isotherms requires so many method-specific image processing steps that these different SNR conditions can be neglected. Finally, a common base for quantitative evaluation of both the tomographic and the spectroscopic experiments would result in an extreme enlargement of the tomographic regions of interest to match the large planar dimensions of the CSI voxels. This would unnecessarily worsen the tomographic results at the expense of a fair comparison between the methods.

For temperature monitoring during hyperthermia treatments (*in vivo*) a lower planar resolution of approximately 1 cm^2 is still sufficient and the acquisition times can be considerably reduced. In addition, various other problems must be solved. Optimizing pulse sequences for one specific tissue can be disadvantageous for tissue species with different MR properties. Pulse sequences with non-optimal parameters can deteriorate the accuracy of mapped temperature distributions. In addition, T_1, D and water PRF based calibration functions deviate from the linear behaviour due to physiological and metabolic changes in tissues during thermal exposure (Lewa and Majewska 1980, Lewa and de Certaines 1995, Young *et al* 1994a, b, MacFall *et al* 1995).

Besides this, there are specific problems related to each MR thermography method itself. Accurate T_1 measurements are difficult and sensitive to inhomogeneities of B_1 field and/or

imperfections of excitation pulses, especially as their frequency blurs in the presence of the slice selection gradients or drifts during heating. Extraction of the temperature induced changes of D is disturbed by motion and perfusion, especially when using conventional pulse sequences. Water PRF based monitoring of temperature changes, which appears at present to be the most promising of all tomographic methods, requires an absolute stability of the static magnetic field or a reliable tracking of the instabilities. Applications of water PRF *in vivo* are also impaired by susceptibility induced phase changes due to deoxyhaemoglobin or myoglobin level shifts mimicing temperature changes (Young *et al* 1996). Furthermore, the two susceptibility constants are temperature dependent as well. The diamagnetic volume susceptibility constant depends on temperature with $0.0026 \times 10^{-6}\,^{\circ}\mathrm{C}^{-1}$ (Weast and Astle 1981), whereby the paramagnetic volume susceptibility constant is inversely proportional to the absolute temperature according to the Curie law (for example Portis 1978). In contrast to the T_1, D and Pr based methods, MR thermography based on the water PRF always requires basal reference measurements. This makes it prone to all kind of misregistration errors. Another drawback of the water PRF method is its apparently lower accuracy in low water content tissues, such as fat, where the screening constant is temperature independent (De Poorter *et al* 1995).

In summary, the water PRF method is the most promising candidate for MRI based thermography. However, the Pr probe with CSI has the potential of improved temperature resolution (even for detection of absolute temperature). Currently, its drawbacks include limited spatial resolution in conjunction with long acquisition times, and the unknown concentration of Pr-MOE-DO3A acceptable in patients for clinical applications. It finally requires advanced MR technology to become a serious rival to the water PRF method (EPI spectroscopic imaging). The D method appears to be inferior to the water PRF method. However, once ultrafast gradients can be provided, this approach should be reconsidered. T_1 based methods, finally, do not appear to be competitive compared with the other methods for non-invasive monitoring in hyperthermia.

Acknowledgment

This work was supported by Deutsche Forschungsgemeinschaft (Sonderforschungsbereich 273 and Graduiertenkolleg 331).

References

Abragam A 1961 *The Principles of Nuclear Magnetism* (Oxford: Clarendon) pp 2–53, 289–305, 566–9

Aime S, Botta M, Fasano M, Terreno E, Kinchesh P, Calabi L and Paleari L 1996 A new ytterbium chelate as contrast agent in chemical shift imaging and temperature sensitive probe for MR spectroscopy *Magn. Reson. Med.* **35** 648–51

Bleaney B 1972 Nuclear magnetic resonance shifts in solution due to lanthanide ions *J. Magn. Reson.* **8** 91–100

Blüml S, Schad L R, Stepanow B and Lorenz W J 1993 Spin–lattice relaxation time measurement by means of a turboFLASH technique *Magn. Reson. Med.* **30** 289–95

Brix G, Schad L R, Deimling M and Lorenz W J 1990 Fast and precise T_1 imaging using a TOMROP sequence *Magn. Reson. Imaging* **8** 351–6

Cetas T C 1984 Will thermometric tomography become practical for hyperthermia treatment monitoring? *Cancer Res.* (suppl) **44** 4805–8

Chung A H, Hynynen K, Colucci V, Oshio K, Cline H E and Jolesz F A 1996 Optimization of spoiled gradient-echo phase imaging for *in vivo* localization of a focused ultrasound beam *Magn. Reson. Med.* **36** 745–52

Cline H E, Hynynen K, Hardy C J, Watkins R D, Schenck J F and Jolesz F A 1994 MR temperature mapping of focused ultrasound surgery *Magn. Reson. Med.* **31** 628–36

Cline H E, Hynynen K, Schneide E, Hardy C J, Maier S E, Watkins R D and Jolesz F A 1996 Simultaneous magnetic resonance phase and magnitude temperature maps in muscle *Magn. Reson. Med.* **35** 309–15

Crawley H J and Henkelman R M 1988 A comparison of one-shot and recovery methods in T_1 imaging *Magn. Reson. Med.* **7** 23–34

De Poorter J 1995 Noninvasive MRI thermometry with the proton resonance frequency method: study of susceptibility effects *Magn. Reson. Med.* **34** 359–67

De Poorter J, De Wagter C, De Deene Y, Thomsen C, Ståhlberg F and Achten E 1994 The proton-resonance-frequency-shift method compared with molecular diffusion for quantitative measurement of two-dimensional time-dependent temperature distribution in a phantom *J. Magn. Reson.* B **103** 234–41

——1995 Noninvasive MRI thermometry with the proton resonance frequency (PRF) method: *in vivo* results in human muscle *Magn. Reson. Med.* **33** 74–81

Dickinson R J, Hall A S, Hind A J and Young I R 1986 Measurement of changes in tissue temperature using MR imaging *J. Comput. Assist. Tomogr.* **10** 468–72

Ernst R R and Anderson W A 1966 Application of Fourier transform spectroscopy to magnetic resonance *Rev. Sci. Instrum.* **37** 93–102

Frenzel T, Roth K, Kossler S, Radüchel B, Bauer H, Platzek J and Weinmann H J 1996 Noninvasive temperature measurement *in vivo* using a temperature-sensitive lanthanide complex and ^{1}H magnetic resonance spectroscopy *Magn. Reson. Med.* **35** 364–9

Gowland P A and Leach M O 1992 Fast and accurate measurements of T1 using a multipoint single inversion recovery sequence *Magn. Reson. Med.* **26** 79–88

Gowland P A and Mansfield P 1993 Accurate measurement of T1 *in vivo* in less than 3 seconds using echo-planar imaging *Magn. Reson. Med.* **30** 351–4

Graumann R, Deimling M, Heilmann T and Oppelt A 1986 A new method for fast and precise T_1 determination *Proc. 5th Ann. Meeting of the Society for Magnetic Resonance in Medicine* (Berkeley, CA: SMRM) pp 922–3

Gubdjartsson H and Patz S 1995 The Rician distribution of noisy MRI data *Magn. Reson. Med.* **34** 910–14

Haase A 1990 Snapshot FLASH MRI: applications to T_1, T_2, and chemical-shift imaging *Magn. Reson. Med.* **13** 77–89

Hall A S, Prior P V, Hand J W, Young I R and Dickinson R J 1990 Observation by MR imaging of *in vivo* temperature changes induced by radio frequency hyperthermia *J. Comput. Assist. Tomogr.* **14** 430–6

Hall L D and Talagala S L 1985 Mapping of pH and temperature distribution using chemical-shift-resolved tomography *J. Magn. Reson.* **65** 501–5

Hentschel M, Dreher W, Wlodarczyk W, Boroschewski R, Röll S A, Wust P, Leibfritz D and Felix R 1998b Fast spectroscopic imaging for noninvasive thermometry using the Pr-MOE-DO3A complex *Proc. 6th Ann. Meeting of the International Society for Magnetic Resonance in Medicine* (Berkeley, CA: ISMRM) p 620

Hentschel M, Wust P, Wlodarczyk W, Frenzel T, Schründer S, Hosten N and Felix R 1998a Noninvasive MR thermometry by 2D spectroscopic imaging of the Pr-MOE-DO3A *Int. J. Hyperth.* **14** 479–93

Hindman J C 1966 Proton resonance shift of water in the gas and liquid states *J. Chem. Phys.* **44** 4582–92

Il'yasov K A and Hennig J 1997 Real time temperature monitoring during hyperthermia sessions with the single shot diffusion weighted RARE sequence *Proc. 5th Ann. Meeting of the International Society for Magnetic Resonance in Medicine* (Berkeley, CA: ISMRM) p 1959

Ishihara Y, Calderon A, Watanabe H, Okamoto K, Suzuki Y, Kuroda K and Suzuki Y 1995 A precise and fast temperature mapping using water proton chemical shift *Magn. Reson. Med.* **34** 814–23

Kay I and Henkelman R M 1991 Practical implementation and optimization of one-shot T_1 imaging *Magn. Reson. Med.* **22** 414–24

Konstanczak P, Schründer S, Schäfer A, Sander B, Frenzel T, Weinmann H-J, Wust P, Müller G and Felix R 1995 Contrast media for localized temperature measurements using proton spectroscopy *Proc. 3rd Ann. Meeting of the Society for Magnetic Resonance* (Berkeley, CA: SMR) p 1110

Kuroda K, Abe K, Tsutsumi S, Ishihara Y, Suzuki Y and Sato K 1993 Water proton magnetic resonance spectroscopic imaging *Biomed. Thermol.* **13** 43–62

Le Bihan D, Dellanoy J and Levin R L 1989 Temperature mapping with MR imaging of molecular diffusion: application to hyperthermia *Radiology* **171** 853–7

Le Roux A and Saint-Jalmes H 1993 A comparison of three different T_1 methods for *in vivo* temperature imaging *Proc. 12th Ann. Meeting of the Society for Magnetic Resonance in Medicine* (Berkeley, CA: SMRM) p 1280

Lewa C J and de Certaines C D 1995 Measurements of the effect of storage at various temperatures on the T_1 of *ex vivo* tissues *Med. Phys.* **22** 831–4

Lewa C J and Majewska Z 1980 Temperature relationships of proton spin–lattice relaxation time T_1 in biological tissues *Bull. Cancer (Paris)* **67** 525–30

Look D C and Locker D R 1970 Time saving in measurements of NMR and EPR relaxation times *Rev. Sci. Instrum.* **41** 250–1

Lutz N W, Kuesel A C and Hull W E 1993 A 1H-NMR method for determining temperature in cell culture perfusion systems *Magn. Reson. Med.* **29** 113–18

MacFall J, Prescott D M, Fullar E and Samulski T V 1995 Temperature dependence of canine brain tissue diffusion coefficient measured *in vivo* with magnetic resonance echo-planar imaging *Int. J. Hyperth.* **11** 73–86

Matsumoto R, Mulkern R V, Hushek S G and Jolesz A 1994 Tissue temperature monitoring for thermal interventional therapy: comparison of T_1-weighted MR sequences *J. Magn. Reson. Imaging* **4** 65–70

Maudsley A A, Oppelt A and Ganssen A 1979 Rapid measurement of magnetic field distribution using nuclear magnetic resonance *Siemens Forsch. Entwick. Ber.* **8** 326–9

Noeske R, Seifert F, Felix R and Rinneberg H 1998 Echo planar spectroscopic imaging (EPSI) at 3 T for non-invasive temperature measurements using the lanthanide complex Pr-MOE-DO3A *Proc. 6th Ann. Meeting of the International Society for Magnetic Resonance in Medicine* (Berkeley, CA: ISMRM) p 1873

Parker D L 1984 Applications of NMR in hypothermia: an evaluation of the potential for localized tissue heating and non-invasive temperature monitoring *IEEE Trans. Biomed. Eng.* **31** 161

Parker D L, Smith V, Sheldon P, Crooks L E and Fussel L 1983 Temperature distribution measurements in two-dimensional NMR imaging *Med. Phys.* **10** 321–5

Pelc N J, Bernstein M A, Shimakawa A and Glover G H 1991 Encoding strategies for three-direction phase-contrast MR imaging of flow *J. Magn. Reson. Imaging* **1** 405–13

Portis A M 1978 *Electromagnetic Fields: Sources and Media* (New York: Wiley)

Prato F S, Drost D J, Keys T, Laxon P, Comissiong B and Sestini E 1986 Optimization of signal-to-noise ratio in calculated T_1 images derived from two spin-echo images *Magn. Reson. Med.* **3** 63–75

Press W H, Teukolsky S A, Vettering W T and Flannery B P 1992 *Numerical Recipes in FORTRAN* 2nd edn (Cambridge: Cambridge University Press)

Saint-Jalmes H 1995 Precision in temperature measurement via T_1 or diffusion imaging *Proc. 3rd Ann. Meeting of the Society for Magnetic Resonance* (Berkeley, CA: SMR) p 1072

Stejskal E O and Tanner J O 1965 Spin diffusion measurements: spin echoes in the presence of a time-dependent field gradient *J. Chem. Phys.* **42** 288–92

Tong C Y and Prato F S 1994 A novel fast T_1-mapping method *J. Magn. Reson. Imaging* **4** 701–8

Vogl T J *et al* 1995 Malignant liver tumors treated with MR imaging-guided laser-induced thermotherapy: technique and prospective results *Radiology* **196** 257–65

Weast R C and Astle M J (ed) 1981 *CRC Handbook of Chemistry and Physics* (Boca Raton, FL: CRC Press)

Webb A G, Wong M, Wilmes L J, Kolbeck K J, Magin R L and Suslick K S 1993 Cobalt-59 functional agents for localized *in vivo* temperature measurements *Proc. 12th Ann. Meeting of the Society for Magnetic Resonance in Medicine* (Berkeley, CA: SMRM) p 245

Wlodarczyk W, Boroschewski R, Hentschel M, Wust P, Mönich G and Felix R 1998a 3D monitoring of small temperature changes for therapeutic hyperthermia using magnetic resonance *J. Magn. Reson. Imaging* **8** 165–74

——1998b 3D MR monitoring of small temperature changes in pelvis *Proc. 6th Ann. Meeting of the International Society for Magnetic Resonance in Medicine* (Berkeley, CA: ISMRM) p 1992

Wust P, Seebass M, Nadobny J, Deuflhard P, Mönich G and Felix R 1996 Simulation studies promote technological development of radiofrequency phased array hyperthermia *Int. J. Hyperth.* **12** 477–94

Wust P, Seebass M, Nadobny J and Felix R 1995 Electromagnetic deep heating technology *Medical Radiology, Principles and Practice of Thermoradiotherapy and Thermochemotherapy* ed M H Seegenschmiedt, P Fessenden and C C Vernon (Berlin: Springer) pp 219–51

Young I R, Hajnal J V, Roberts I G, Ling J X, Hill-Cottingham R J, Oatridge A and Wilson J A 1996 An evaluation of the effects of susceptibility changes on the water chemical shift method of temperature measurement in human peripheral muscle *Magn. Reson. Med.* **36** 366–74

Young I R, Hand J W, Oatridge A and Prior M V 1994b Modeling and observations of temperature changes *in vivo* using MRI *Magn. Reson. Med.* **32** 358–69

Young I R, Hand J W, Oatridge A, Prior M V and Forse G R 1994a Further observations on the measurement of tissue T_1 to monitor temperature *in vivo* by MRI *Magn. Reson. Med.* **31** 342–5

Zhang Y, Samulski T V, Joines W T, Mattiello J, Levin R L and Le Bihan D 1992 On the accuracy of noninvasive thermometry using molecular diffusion magnetic resonance imaging *Int. J. Hyperth.* **8** 263–74

Zuo C S, Bowers J L, Metz K R, Nosaka T, Sherry A D and Clouse M E 1996 $TmDOTP^{5-}$: a substance for NMR temperature measurements *in vivo Magn. Reson. Med.* **35** 648–51